Analytical prediction of texture of multi-phase materials in laser powder bed fusion

Wei Huang[1*], Hamid Garmestani[2] and Steven Y. Liang[1*]

[1*]George W. Woodruff School of Mechanical Engineering, Georgia Institute of Technology, 801 Ferst Drive, Atlanta, 30332, GA, USA.
[2]School of Materials Science and Engineering, Georgia Institute of Technology, 771 Ferst Drive NW, Atlanta, 30332, GA, USA.

*Corresponding author(s). E-mail(s): whuang378@gatech.edu; steven.liang@me.gatech.edu;
Contributing authors: hamid.garmestani@mse.gatech.edu;

Abstract

Crystallographic orientations are critical in determining material properties among all microstructure representations due to their influence on anisotropy, void growth, coalescence behaviors, etc, in laser powder bed fusion (LPBF). This work developed a physics-based analytical model to predict the multi-phase materials texture related to the 3D temperature distribution, considering heat transfer boundary conditions, heat input using point-moving heat source solution, and heat loss due to heat conduction, convection, and radiation. This study offers a quick and more precise way of analyzing texture prediction in multi-phase mode for metallic materials. It lays the groundwork for future research on microstructure-affected or texture-affected materials properties in academic and industrial settings. This study initially employs a computational approach to generate a singular BCC beta phase texture based on thermal history to represent the liquidus materials of Ti-6Al-4V during the melting process. Then, the multi-phase texture is constructed by using Bunge calculation. Additionally, the effect of scanning strategy and processing parameters on texture are investigated.

Keywords: Laser Powder Bed Fusion & Analytical Modeling; Boundary Heat Transfer & 3D Temperature Prediction; Texture & Multi-Phase Materials

1 Introduction

Richard P. Feynman suggested plenty of room at the bottom in 1959 [1], alluding to the possibility of operating at smaller sizes. This statement inspired many of the research areas that continue to this day: nanotechnology fields, characterization facilities, manufacturing, molecular engineering [2], etc. The talk aims to motivate exploration on a smaller scale. However, fabrication issues arise when operating at these scales. Materializing AM is suitable for tackling them, using the addition philosophy based on physical rules. Moreover, if physically permitted, new paradigms could lead to breakthroughs in operating on smaller scales of atoms, quarks, and beyond, propelling human civilization to new heights. By adhering to physical laws and developing novel paradigms, Additive Manufacturing (AM) presents a viable alternative that may pave the way for advancements in atomic and subatomic operations. These days, AM is widely acknowledged as a new paradigm for producing high-performance parts for a range of

applications in the automotive, energy, aerospace, and medical fields [3]. AM offers many advantages, but it also has a lot of disadvantages, such as anisotropic mechanical and microstructure properties, a small selection of materials, defects like porosity, and expensive expenses. Different mechanisms are involved in printing technology and novelly structured materials. Quick progress will make more research necessary before implementing in industrial applications, involving a wider range of materials and procedures. An appropriate substitute for the finite element method and conventional experiments is a physics-based analytical approach because of the high costs, anisotropy, scaling problems, and related challenges.

Since anisotropy is critical, texture or grain orientation distribution must be investigated. Numerous research papers have employed numerical models, experimental techniques, and machine learning to forecast the microstructure of materials or characterize the evolution of microstructures due to various factors such as processing conditions and original material properties. A physical-based single-phase texture analytical model has been created by W. Huang et al. [4], which takes into account heat losses through conduction, convection, and radiation in a three-dimensional heat transfer boundary condition while determining thermal profile in LPBF. Then, the multi-phase texture is constructed using Bunge calculation and the columnar-to-equiaxed transition (CET) principle [5]. Furthermore, in addition to validating the texture models, the investigation of processing parameters, including laser power and scanning speed, and scanning strategies, such as number of layers and rows scanned, are also explored in this work.

2 Methodology

2.1 Thermal profile

Predicting the heat profile that arises from the laser therapy is the first stage in the modeling procedure. The following simulations of several elements, including texture, grain size, thermal stress, residual stress, etc., are based on this prediction. This work should make use of the physical-based single-phase texture analytical model developed by W. Huang et al. [4], which took into account heat losses by conduction, convection, and radiation in a three-dimensional heat transfer boundary condition when determining thermal profile. A closed-form solution is used to incorporate the boundary conditions of heat transfer since geometry is crucial in real-world applications. The boundary faces have been divided into many heat sinks with equal areas in order to calculate heat loss. The 3D thermal profile is best expressed as follows:

$$\begin{aligned} T(x,y,z) = & \frac{1}{4\pi kR}\left(P\eta \exp\left(-\frac{V(R+x)}{2\kappa}\right)\right. \\ & \left. - A\left(h(T-T_0)+\varepsilon\sigma(T^4-T_0^4)+\frac{k_p(T-T_0)}{R}\right)\right)+T_0 \end{aligned} \tag{1}$$

$$\kappa = K/\rho c \tag{2}$$

$$R^2 = (x-x_0)^2+(y-y_0)^2+(z-z_0)^2 \tag{3}$$

where η is the laser absorption coefficient, κ is thermal diffusivity, ρ is density, V is laser scanning velocity, P is laser power, K is thermal conductivity, and c is heat capacity. The distance between the heat source and the analysis point is represented by the symbol R. k_p represents the thermal conductivity of the powder, h the heat convection coefficient, ε the emissivity, σ the Stefan-Boltzmann constant, A the area of each heat sink on the melt pool surface, and T the simulated thermal profile.

2.2 Texture

For the single-phase BCC structure of Ti-6Al-4V, three Euler angles, in Bunge convention, represent the crystallographic orientation in each grain, defining the rotations required to transform from the lab reference frame to the crystallographic lattice frame.

Concerning the multi-phase texture, the CET model illustrated by a specific ratio value $\emptyset$ in the $G-R_S$ space [6] was utilized. The substrate was a polycrystalline powder with several random orientations, and the solidification area featured columnar grains that grew epitaxially from the seed crystal. The direction of growth of the terminal dendrite at a specific location point can be determined by maximizing the cosine value of the angle created by two vectors.

$$G = |\nabla T| \tag{4}$$

$$R_S = V \cos\theta \tag{5}$$

$$G - R_S(Ratio) = \frac{G^n}{R_S} \tag{6}$$

$$\cos\phi = \frac{\boldsymbol{m} \cdot \boldsymbol{G}}{\boldsymbol{G}} \tag{7}$$

where V is the scanning speed, G is the thermal gradient, R_S is the solidification rate, and θ is the angle between the scanning and growth directions. $\cos\phi$ has a maximum value that is determined by the crystallographic orientation vector $\boldsymbol{m}$ of the unique seed crystal. $\boldsymbol{G}$ is the temperature gradient vector at this point.

For Ti-6Al-4V, the alpha HCP, the second phase was anticipated to position itself [7], but concerning the father texture. The relationship between growth rate and thermal gradients (G vs. R_S) can be mapped [8], and the relative distributions of six distinct types of alpha-phase precipitates can be accurately determined [9].

3 Results and discussion

3.1 Thermal profile

The initial step involves establishing the thermal profile as the foundation. The model's input, which includes material properties of Ti-6Al-4V, processing parameters, and part geometry information, is clarified and listed in Table 1. As for validating the model by comparing it to the experimental data, W. Huang et al. [4] have done that, which is skipped here.

3.2 Texture

Before exploring the influence of processing parameters on the simulated texture, it is important to finish the validations of the single-phase texture and multi-phase texture models.

3.2.1 Single-phase Texture

Fig. 1 refers to the validation of the single-phase texture model by comparing the texture intensity of ¡100¿ direction between the experimental result and the simulated one, as completed in the previous work. The processing parameters of laser power and scanning speed are fixed at 157 W and 225mm/s, respectively. The building settings are listed in Table 2. The locations of the high-intensity peaks and their values are comparable.

Table 1 Materials Properties and Values of Ti-6Al-4V [10][11][12][13] and Part Geometry Settings

Model Inputs	Value	Unit
Surrounding Temperature (T_0)	20	°C
Melting Temperature (T_m)	1655	°C
Density (ρ)	4428	kg/m^3
Modulus of Elasticity (E)	60.78	GPa
Poission's Ratio (ν)	0.34	1
Bulk Thermal Conductivity (k_t)	5-35	$W/(mK)$
Powder Thermal Conductivity (k_p)	0.21	$W/(mK)$
Heat Capacity (C)	500-800	$J/(KgK)$
Heat Convection Coefficient (h)	24	$W/(m^2K)$
Radiation Emissivity (ε)	0.9	1
Stefan-Boltzmann Constant (σ)	5.67×10^{-8}	$W/(m^2K)$
Columnar/Equiaxed Transition Coefficient (nn)	3.2	1
Columnar/Equiaxed Transition Coefficient (kk)	10^{25}	1
Laser Absorption Value	0.818	1
Part Length (L)	4	mm
Part Width (W)	1	mm
Part Height (H)	0.5	mm
Number of Heat Sinks (S)	9	1
Layer Thickness	50	μm
Hatching Space	50	μm

Table 2 Build Settings

Parameters	**Value**	**Unit**
Layers	10	1
Seeds	100	1
Sections	1000	1
Grains	20	1
Track	1	1

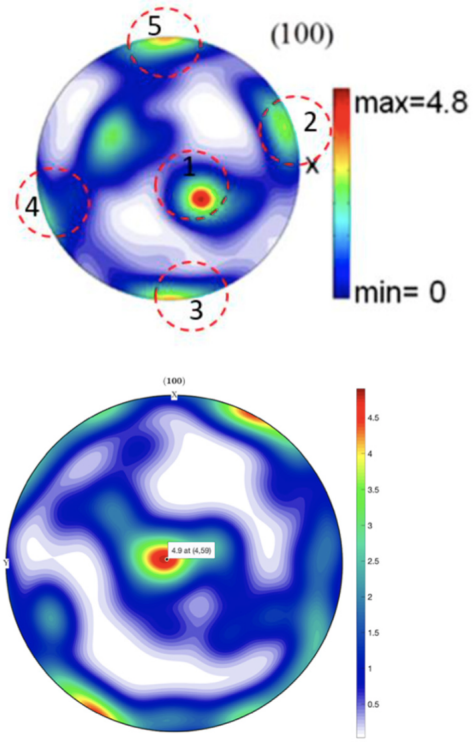

Fig. 1 Referred validation figure of single-phase texture model of Ti-6Al-4V in LPBF [4]: the top figure is the experimental result and the bottom figure is the simulated result.

3.2.2 Multi-phase Texture

As indicated in the methodology, to imitate the alpha-phase hexa HCP texture precipitates, the following formulas demonstrate the frequency recording of the six alpha-phase precipitates rotational matrices and their distributions applied to the single-phase BCC texture of the materials. With a slight random variation of 0.38%, the simulation fixed the volume ratio between the beta- and alpha-titanium crystalline phases at 85:15.

$$\mathbf{D}^{-1}\mathbf{E} = \begin{bmatrix} 1 & 0 & 0 \\ 0 & 1 & 0 \\ 0 & 0 & 1 \end{bmatrix} \quad (17.8\%) \tag{8}$$

$$\mathbf{D}^{-1}\mathbf{C}^{23+} = \begin{bmatrix} \frac{1}{2} & \frac{\sqrt{3}}{2} & 0 \\ \frac{\sqrt{3}}{2} & -\frac{1}{2} & 0 \\ 0 & 0 & -1 \end{bmatrix} \quad (13.2\%) \tag{9}$$

$$\mathbf{D}^{-1}\mathbf{C}^{3z+} = \begin{bmatrix} -\frac{1}{2} & -\frac{\sqrt{3}}{2} & 0 \\ \frac{\sqrt{3}}{2} & -\frac{1}{2} & 0 \\ 0 & 0 & -1 \end{bmatrix} \quad (11.3\%) \tag{10}$$

$$\mathbf{D}^{-1}\mathbf{C}^{21+} = \begin{bmatrix} 1 & 0 & 0 \\ 0 & -1 & 0 \\ 0 & 0 & -1 \end{bmatrix} \quad (14.4\%) \tag{11}$$

$$\mathbf{D}^{-1}\mathbf{C}^{22+} = \begin{bmatrix} -\frac{1}{2} & \frac{\sqrt{3}}{2} & 0 \\ \frac{\sqrt{3}}{2} & \frac{1}{2} & 0 \\ 0 & 0 & -1 \end{bmatrix} \quad (16.9\%) \tag{12}$$

$$\mathbf{D}^{-1}\mathbf{C}^{6z+} = \begin{bmatrix} \frac{1}{2} & -\frac{\sqrt{3}}{2} & 0 \\ \frac{\sqrt{3}}{2} & \frac{1}{2} & 0 \\ 0 & 0 & 1 \end{bmatrix} \quad (26.4\%) \tag{13}$$

As the Fig. 2 suggests, the simulated dual-phase pole figures support the basic propensity and creation of the two phases, which are in good agreement with what has been reported in the prior literature [14][15]. The intensity peak of (100), (011), and (-111) shows that the BCC phase lacks a central node but has discrete nodes in each of the three planes. The HCP phase exhibits a prominent center intensity in the (0001) direction, while the intensities for the other orientations extend to the boundaries of the other pole figures.

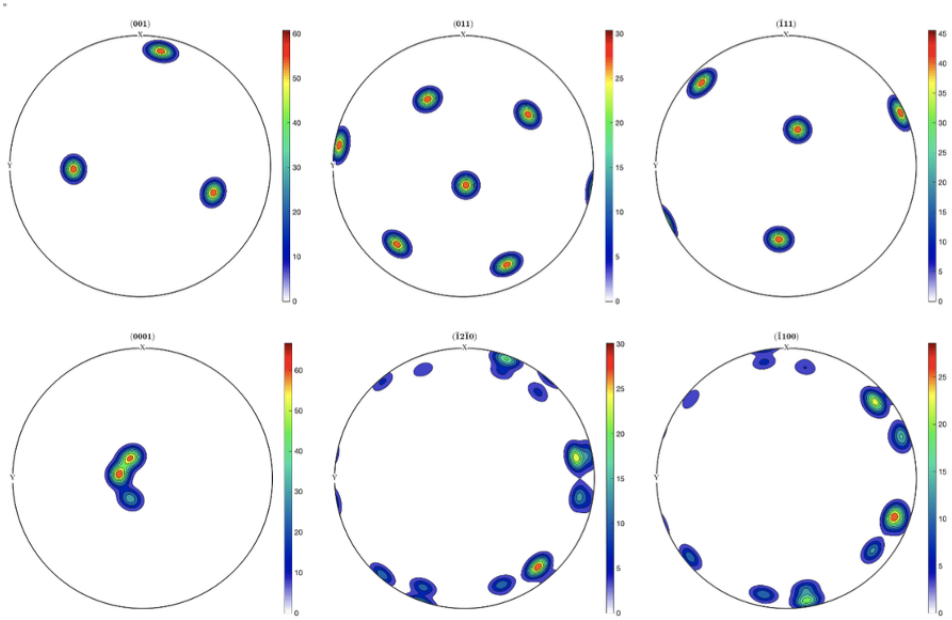

Fig. 2 Pole figures of the dual-phase Ti-6Al-4V texture were simulated. The BCC phase is shown in the first row and the HCP phase in the second.

3.2.3 Influence of Processing Parameters on Texture

With the validated analytical multi-phase texture model, it is now possible to analyze the crystalline orientation quickly and relatively accurately with various processing factors such as scanning strategy, laser power, and part geometry. Thus, in the following, some variations of processing parameters are made to give rise to some prediction, new knowledge, or trend of the resultant texture.

First, the laser power is changed to investigate its influence on the multi-phase texture. The previous experiments and simulation for validation used 157 W and 225 mm/s as processing inputs. Then, while the scanning speed and all of the other parameters, the laser power is adjusted to 200 W, 250 W, and 300 W. The simulated BCC phase and HCP phase of the three different settings are presented in Fig. 3 and Fig. 4.

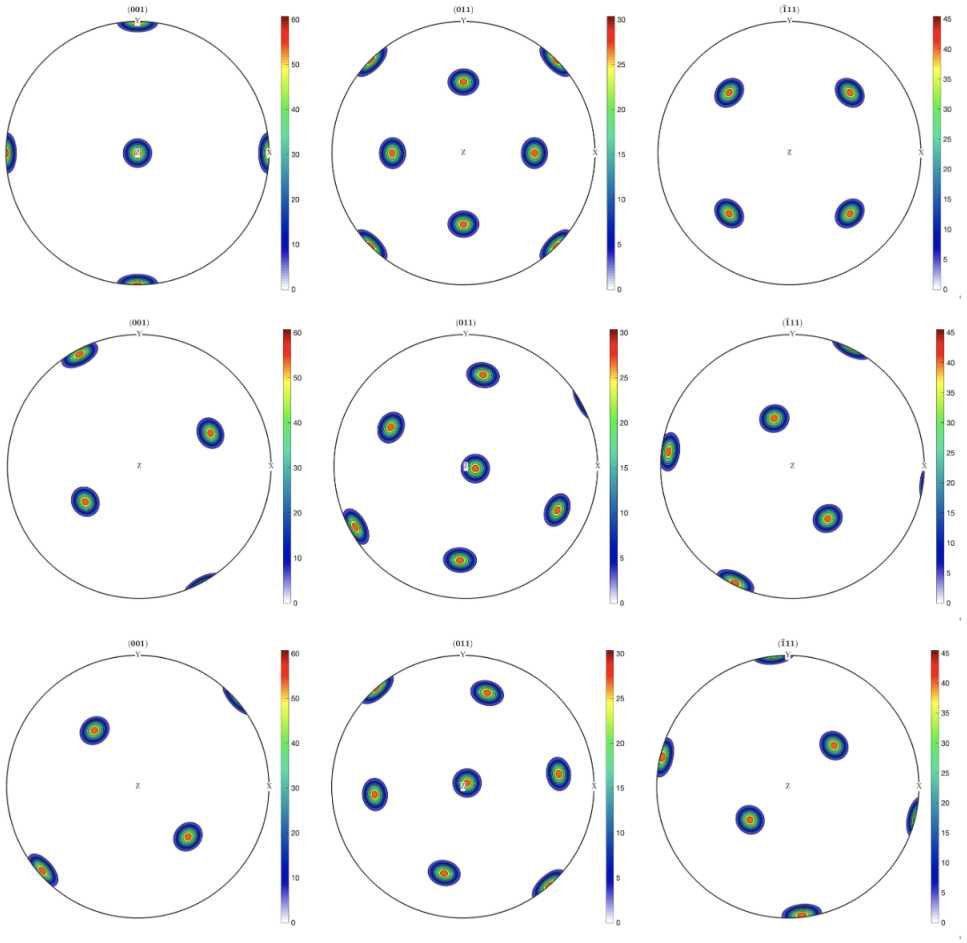

Fig. 3 BCC phase pole figures of the dual-phase Ti-6Al-4V texture. From top to bottom: 200 W, 250 W, 300 W, while the scanning speed is kept at 225mm/s.

In these three cases with changed laser power regarding the BCC phase, the intensity peak of (100), (011), and (-111) does not show the same trend that it lacks a central node but has discrete nodes in each of the three planes, but instead, in the setting of 200 W; the node appears in the center of the (100) pole figure while the other two planes also have their four nodes in very symmetry places though the other two cases still show discrete nodes in three planes. With this finding, the case of 200 W is a suitable setting for processing parameters that could be applied in an actual situation.

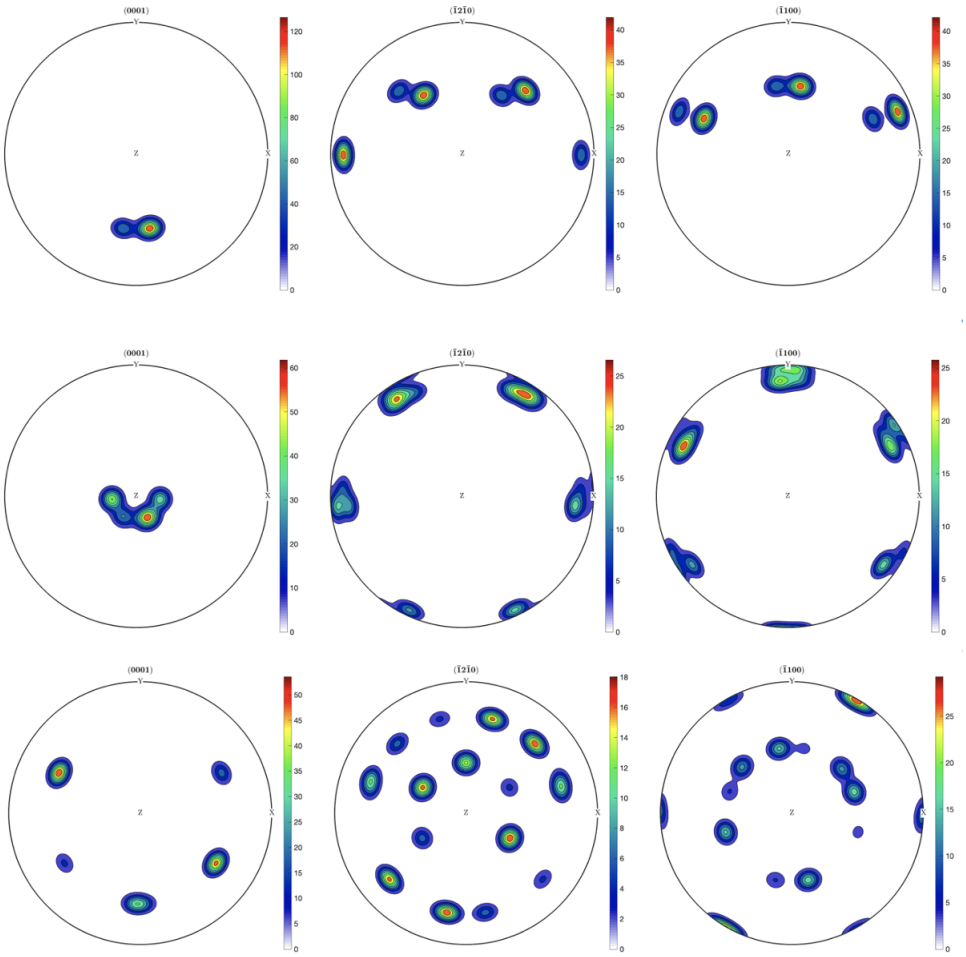

Fig. 4 HCP phase pole figures of the dual-phase Ti-6Al-4V texture. From top to bottom: 200 W, 250 W, 300 W, while the scanning speed is kept at 225mm/s.

Similarly, the HCP phase simulated results with changed laser power also present different propensities. For (0001), the center intensity moves downward in the 200 W case, and it extends outward in the 300 W case, while the 250 W case is kept in the center. The intensities for the other orientations spread to the boundaries of the other pole figures similarly, though to different degrees.

The mechanism of altering the scanning speed is similar to that of laser power, mainly influencing the energy absorbed by the materials, so we do not explore the effect of the scanning speed for its influence on multi-phase texture. However, the scanning strategy should be investigated. This work has three different strategy simulation sets, where the number of scanned rows and layers, (rows, layers), varies from (3, 3) to (4, 4) to (5, 5), with the laser power and scanning speed invariable at 157 W and 225 mm/s. The layer thickness and hatching space are both 50 μm. The simulated BCC phase and HCP phase of the three different settings are presented in Fig. 5 and Fig. 6.

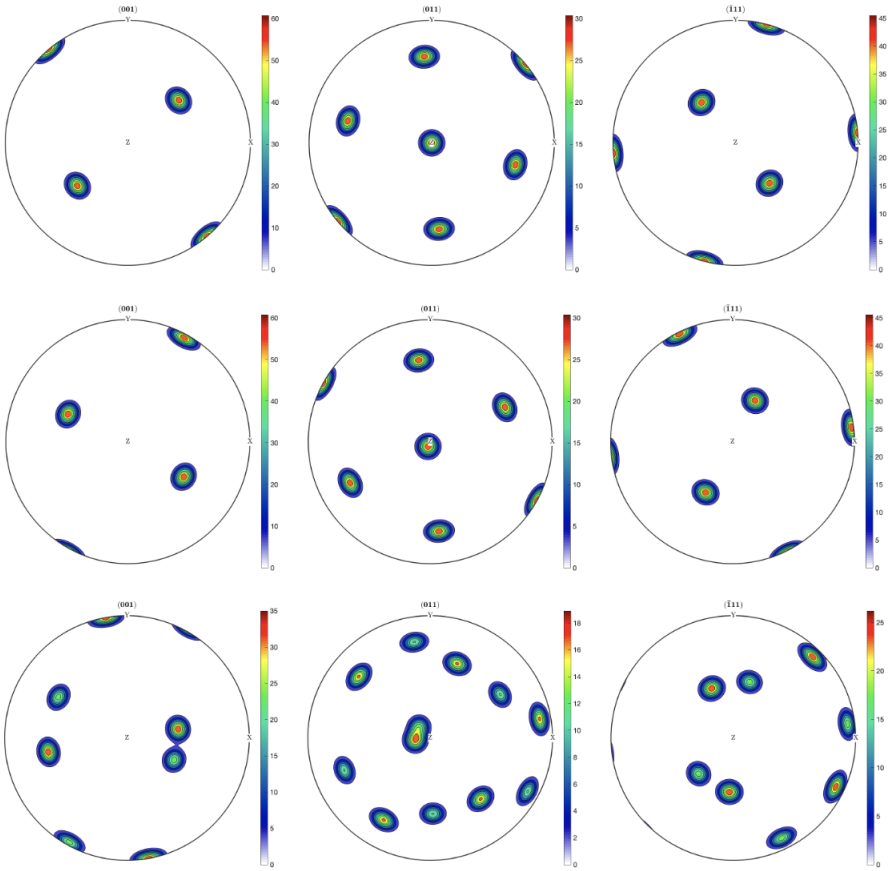

Fig. 5 BCC phase pole figures of the dual-phase Ti-6Al-4V texture. From top to bottom: three rows and three layers, four rows and four layers, five rows and five layers.

In the three cases with altering scanning strategies regarding the BCC phase, similarly, the intensity peak of (100), (011), and (-111) does not show the same tendency that it lacks a central node but still has discrete nodes in each of the three planes. This also tells that the scanning strategy can affect the texture of the BCC phase pole figures with similar discrete patterns.

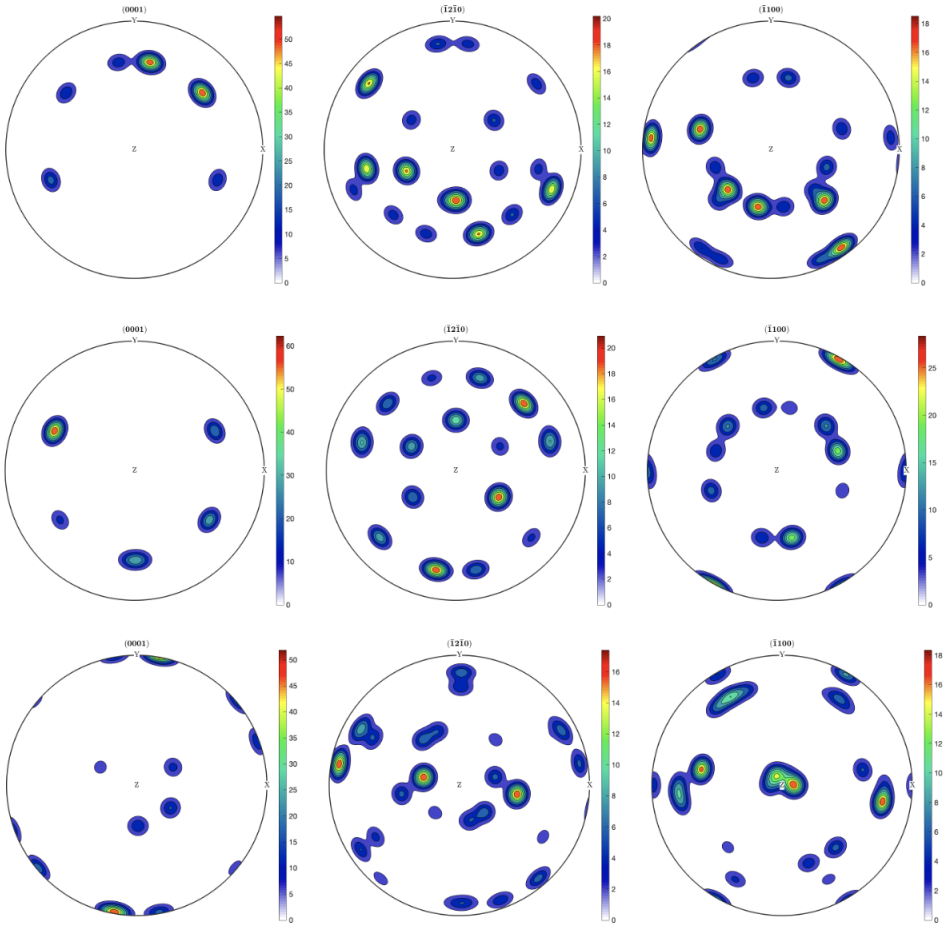

Fig. 6 HCP phase pole figures of the dual-phase Ti-6Al-4V texture. From top to bottom: three rows and three layers, four rows and four layers, five rows and five layers.

The HCP phase simulated results with adjusted scanning strategies, and they again present different propensities. For (0001), the center intensity is replaced by a small circle of weak intensities in all three situations. The intensities for the other orientations do not spread to the boundaries but instead disperse in their figures.

4 Conclusions

Due to disadvantages such as anisotropy and the high cost that additive manufacturing currently faces, physics-based analytical models are established for rapidly simulating multi-phase texture, and the influence of processing parameters, including laser power and scanning strategy, on texture is explored in this work. Firstly, a physical-based single-phase texture analytical model is developed to consider heat losses through conduction, convection, and radiation in a 3D heat transfer boundary condition while determining the thermal profile in LPBF. The multi-phase texture is created using Bunge calculation and the CET principle. Moreover, the models are validated by comparing past experimental data. Likewise, in addition to validating the texture models, the processing parameters were investigated by changing the laser power and the number of rows and layers scanned in each simulation setting.

The validations show the accuracy and robustness of this research's built analytical texture model. Additionally, the investigation of processing parameters reveals several lessons. Laser power, scanning speed, and the scanning strategy of the layers and rows scanned can affect the texture output, though the limited cases in this work have not found specific tendency rules. Among the several processing parameter settings, 200 W and 225 mm/s show symmetry and clear patterns regarding the nodes in the

pole figures. Besides, the texture models indeed provide a fast-modeling way, demonstrating the potential of shrinking the high cost generally spent in experimental methods and searching out more optimized processing parameters settings that are of great value at a fast pace.

Acknowledgements

This work was supported by the Boeing Company.

Declaration of Competing Interest

The authors declare that they have no known competing financial interests or personal relationships that could have appeared to influence the work reported in this paper.

References

[1] Feynman, R.P.: Plenty of room at the bottom. In: APS Annual Meeting, pp. 1–7 (1959). Little Brown Boston, MA, USA

[2] Drexler, K.E.: Molecular machinery and manufacturing with applications to computation. PhD thesis, Citeseer (1991)

[3] DebRoy, T., Wei, H., Zuback, J., Mukherjee, T., Elmer, J., Milewski, J., Beese, A.M., Wilson-Heid, A.d., De, A., Zhang, W.: Additive manufacturing of metallic components–process, structure and properties. Progress in Materials Science **92**, 112–224 (2018)

[4] Huang, W., Wang, W., Ning, J., Garmestani, H., Liang, S.Y.: Analytical model of quantitative texture prediction considering heat transfer based on single-phase material in laser powder bed fusion. Journal of Manufacturing and Materials Processing (2024)

[5] Hunt, J.D.: Steady state columnar and equiaxed growth of dendrites and eutectic. Materials science and engineering **65**(1), 75–83 (1984)

[6] Kobryn, P.A., Semiatin, S.L.: Microstructure and texture evolution during solidification processing of ti–6al–4v. Journal of Materials Processing Technology **135**, 330–339 (2003)

[7] Simonelli, M., Tse, Y.Y., Tuck, C.: On the texture formation of selective laser melted ti-6al-4v. Metallurgical and Materials Transactions A **45**, 2863–2872 (2014)

[8] Al-Bermani, S.S., Blackmore, M., Zhang, W., Todd, I.: The origin of microstructural diversity, texture, and mechanical properties in electron beam melted ti-6al-4v. Metallurgical and Materials Transactions A **41**, 3422–3434 (2010)

[9] Glavicic, M.G., Kobryn, P.A., Bieler, T.R., Semiatin, S.L.: An automated method to determine the orientation of the high-temperature beta phase from measured ebsd data for the low-temperature alpha-phase in ti–6al–4v. Materials Science and Engineering A-structural Materials Properties Microstructure and Processing **351**, 258–264 (2003)

[10] Yang, Y., Knol, M.F., Keulen, A., Ayas, C.: A semi-analytical thermal modelling approach for selective laser melting. Additive manufacturing **21**, 284–297 (2018)

[11] Gusarov, A.V., Yadroitsev, I., Bertrand, P., Smurov, I.Y.: Model of radiation and heat transfer in laser-powder interaction zone at selective laser melting. Journal of Heat Transfer-transactions of The Asme **131**, 072101 (2009)

[12] Boyer, R.R., Welsch, G., Collings, E.W.: Materials properties handbook: Titanium alloys. (1994). https://api.semanticscholar.org/CorpusID:137221408

[13] Yadroitsev, I., Yadroitsava, I.: Evaluation of residual stress in stainless steel 316l and ti6al4v samples produced by selective laser melting. Virtual and Physical Prototyping **10**, 67–76 (2015)

[14] Muiruri, A.M., Maringa, M., Preez, W.B.: Crystallographic texture analysis of as-built and heat-treated ti6al4v (eli) produced by direct metal laser sintering. Crystals (2020)

[15] Takajo, S., Tomida, T., Caspi, E.N., Pesach, A., Tiferet, E., Vogel, S.C.: Property improvement of additively manufactured ti64 by heat treatment characterized by in situ high temperature ebsd and neutron diffraction. Metals (2021)